LAWRENCE
LIVERMORE
NATIONAL
LABORATORY

LLNL-TR-665420

HERMES Model Developments and Status to Support Simulations and Analyses of XDT and DDT

J. E. Reaugh

December 16, 2014

Disclaimer

This work performed under the auspices of the U.S. Department of Energy by Lawrence Livermore National Laboratory under Contract DE-AC52-07NA27344.

HERMES Model Developments and Status to Support Simulations and Analyses of XDT and DDT

John E. Reaugh
December 11, 2014

1. Model requirements for XDT

1.1 Introduction

The phenomenon of XDT (unknown Detonation Transition) has been studied experimentally for many years, but computer simulations have been rare. We seek to build on successful applications of the HERMES model to HEVR (High Explosive Violent Response) including DDT (Deflagration to Detonation Transition) and SDT (Shock to Detonation Transition). In HEVR, the pressure developed in the explosive is relatively low and not all the explosive is consumed. If conditions are right, however, HEVR can build up pressure quickly enough to develop a detonation in the remaining explosive via DDT.

The mechanical insults that lead to XDT are relatively strong, but not so strong that SDT results. The geometries that lead to XDT are lightly confined, so that the explosive fragments and develops porosity. Unlike DDT and SDT, it is typical for XDT response to be stochastic. For nominally identical experiments, violent reactions (detonations) occur only some of the time. From results such as these, we infer that for a given geometry and insult there is a relatively small combination of fragmentation and porosity ("sweet spot") for which ignition develops and grows to detonation. Some experiments develop a small, expanding cloud of fragments that intercepts a nearby surface. Ignition (if it happens) starts at that surface. If conditions are right, the ignition propagates back through the cloud and detonates the remaining charge.

For a given geometry and nominal impact condition, XDT may be rare. The consequences are large, because in those few cases, the entire charge is consumed. The study of XDT, then, is important for safety-related analyses.

1.2 Experimental scenarios leading to XDT

Early instances of scenarios leading to XDT in propellants appeared in the 7th Detonation Symposium. Keefe [1] observed a delayed detonation sometimes occurring in the gap test when using more cards (reduced shock pressure) than needed to prevent prompt detonations (0 detonations in 9 or 10 trials). These delayed detonations were observed with as much as 70% probability, and decreased to zero with additional cards. Jensen [2] reported results from a shotgun test, velocity range 400 to 1000 m/s, which resulted in XDT about 25% of the time. He also reported results for the pick-up test, where the shotgun-launched propellant hit a disk of the same propellant before both impacted the steel target plate. In the same velocity range, this geometry also resulted in 25% XDT. Green [3] presented results at lower velocity, 150 to 300 m/s, using a heavy steel projectile to impact a propellant cylinder. He later [4] extended his test configuration to

include both hollow cylinders and two cylinders spaced along the projectile shot axis, which were hit with the same projectile sequentially.

Later, Salvetat [5] and Bernecker [6] reported results in the 10th Symposium similar to [1] for gap tests. Their tests also used propellants. Guengot [7] replicated Keefe's results (with what may have been the same propellant), but in addition presented results from double gap tests, with two donor charges at opposite ends of the propellant acceptor cylinder. The donor charges were detonated sequentially with a delay that he varied. Guengot noted that when he removed the steel tube confinement from the geometry of [1], no XDT resulted for card gap thicknesses in the range where the steel-confined propellants showed XDT. The consensus for XDT in the gap test is that the first shock from the donor charge fragments the acceptor charge. The reflected shock in the acceptor charge, after a portion of that charge crosses the small gap and impacts the steel base plate, runs back to detonation in the fragmented, porous acceptor.

Finnegan [8] presented a summary of work performed in the late 1980's and early 1990's using two plates of propellant separated by a gap, which he called the planar rocket motor (subsequently referred to as BVR and ABVR tests). This is a geometric simplification of the scenario where a single fragment impacts the side of a rocket motor. The gap between the plates represents the central bore of the motor. The response spectrum comprises no reaction through delayed detonation, depending on the projectile velocity (typically in the range 1000 to 1300 m/s), gap spacing, and propellant.

Haskins [9] presented results for the impact of a single steel cylinder, L/D about 2, velocity range 1000 to 2000 m/s, impacting explosive cylinders of various diameters, some with steel confinement, and with either metallic cover plates or bare-faced cylinders. Some of the impacts resulted in XDT. Small diameter explosive cylinders and no lateral confinement fostered XDT. Later, Cook [10, 11] presented results for larger diameter explosive cylinders that were impacted by cylindrical projectiles with conical, rather than flat-ended, noses so that SDT was not observed. In those tests, the shower of fragments (velocity range 300 to 500 m/s) from the back face impacted a steel plate. The response spectrum comprises no reaction through prompt reaction, including detonation, depending on the spacing between the back face and the steel plate. If the spacing is either too close or too distant, the result is no reaction. The velocity of the incoming steel fragment needed to be greater than about 1600 m/s to obtain XDT.

Recently Haskins [12] presented results for the impact of two steel spheres on an HE cylinder with steel confinement, and both with and without a metallic cover plate. The spheres were fired from the same gun with a single propellant load, but the sabot design permitted the spheres to be offset laterally in space and also in time. He observed conditions for which XDT occurred.

Burn tube experiments [13, 14], although sometimes described as DDT, might better be considered XDT tests. The geometry is a steel tube with thick steel end caps threaded on. In those tests, performed on high-density explosives, a small amount of propellant is ignited near one end, in a volume that provides ullage. The burning of the igniter propellant is rapid enough to deliver a compressive shock into the solid explosive. The shock then reverberates several times through the charge, causing fractured explosive that can move into the ullage, thereby creating porosity. The hot propellant gas is adequate to

ignite one end of the charge. Flame may progress into the broken explosive, or between the explosive and the tube wall [14]. A violent event (which we are here considering to be XDT) sometimes results.

It is possible that in some cases the occasional violent response of a cook-off test may be due to XDT. Here we imagine that a localized thermal run-away develops enough pressure, and with a rapid enough rise time, that stress waves propagated into the warm, but not burning, explosive introduce fractures. If porosity can also develop, due to confinement expansion, then similarly to the burn tube observations, a DDT or SDT may result.

1.3 Assessment of the various scenarios

Participants in a workshop convened by NIMIC and held at NAWC China Lake [15], agreed on a definition of XDT: "*The transition to detonation by a compression, release, recompression process as the result of a single initial stimulus*." This would seem to rule out the recent double sphere experiments of Haskins [12], which should probably not be ruled out. It also rules out SDT or DDT of an initially porous bed, which is reasonable, since they are in fact well described as such. Nevertheless, it is clear that the phenomena of SDT and DDT in porous beds are closely related to XDT.

In all the scenarios described above, the compression followed by release results in fragmentation and porosity. If the recompression is a shock, such as occurs when a shower of fragments is intercepted by a propellant (or steel) plate, then a shock may develop that is strong enough to lead to detonation (SDT) in the distance afforded by the fragment shower. If not, the reactive shock may still be strong enough to run to detonation in the remaining charge. If the recompression is not a shock, for example the single projectile experiments of Haskins, the delayed response might be started by an ignition caused by shear localization near the projectile, then followed by a build-up to detonation.

Results from the single projectile experiments of Haskins, the gap test, and most others, suggest to us that there is a specific "sweet spot" in fragmentation and porosity space that is needed to produce delayed detonation or XDT. The ratio of steel wall thickness to explosive diameter is the same for Haskins' projectile tests and Keefe's gap tests. Haskins found that the steel prevented XDT, but Guengot found that removing the steel prevented XDT. Clearly not only the confinement, but also the stimulus matters for creating fragmentation and porosity in the "sweet spot." None of the gap test results on propellants described the propellant composition, let alone the mechanical properties needed to assess fragmentation. There was the statement that some propellants were more susceptible to XDT than others. These observations lead us to suppose that a model for XDT will require accurate submodels for the development of fragment size and porosity.

The shotgun and pick-up test results described by Jensen had two interesting features. 1) The air blast measured for XDT (delayed response) exceeded the air blast measured for SDT (prompt response), and the air blast measured for the pick-up test XDT was higher than would be accounted for by just the mass of the extra disk relative to the 8-gram propellant cylinder. 2) On average, only 25% of the tests resulted in XDT. We tentatively

assume that the low blast pressure measured from SDT was because the detonation started, but then failed. (The critical diameter was not specified). We assume that the XDT blast pressure was the result of only a portion of the 8-gram cylinder fragmenting and remaining near enough to burn, but more propellant mass was involved than the detonation consumed in the SDT cases. We also assume that the disk of propellant in the pick-up tests was fragmented, and still more of the 8-gram cylinder was fragmented. The baseline measurement of detonating the 8-gram sample or 8-gram sample plus disk was not reported. We further hypothesize that the reason only a small fraction of the tests resulted in XDT is that the "sweet spot" is small. The uncontrolled and unmeasured tilt/yaw at impact may cause large enough changes to fragmentation and porosity that only a few of the tests resulted in XDT.

We note that for some tests and some investigators, the criterion for deciding whether a detonation occurred was imprecise. Air blast, alone, does not distinguish detonation from explosion. The peak pressure in the energetic material during an explosion is typically an order of magnitude (or more) smaller than the peak pressure in the material during a detonation, although each test results in the same far-field air blast signal. On the other hand, the appearance or fragment size of adjacent steel fixtures can distinguish the higher pressure and faster loading rate of a detonation from the smaller pressure and slower loading rate of an explosion. From a safety-related perspective, both detonations and explosions create the same far-field damage from air blast. The near-field damage caused by shock strength will be quite different.

The fragment cloud experiments of Cook [10, 11] were performed on a number of different explosives, including TNT, RDX-, and HMX-based explosives, and also on AP-based propellants. He has not tested TATB-based explosives. He observed [16] that there were at least three modes of ignition that then, depending on conditions, would spread to the remaining cloud and also the unfragmented explosive. They include friction and jetting when the cloud intercepts a lateral boundary, pinch when the cloud is squeezed against the back plate by the projectile, and reshock when the cloud intercepts the back plate. We provisionally assume that the ignition from shear localization in HERMES can describe both friction/jetting and pinch ignitions, and that the CREST-lite SDT ignition in HERMES can describe reshock ignition. Although friction/jetting were observed on the back plate, especially near the go/no-go threshold, they were only seen with no-go's. Cook also observed that for some explosives the fragmentation was severe enough that individual explosive crystals were part of the fragment cloud.

The varied response of the same explosive in the burn tube tests suggests to us that this is best considered XDT. Here again, the fragmentation and porosity must be in the "sweet spot" for a violent reaction to occur. In this test the appearance of the steel confining tube is used to determine whether the response was a pressure burst, explosion, or detonation.

1.4 Assessment of model requirements

1.4.1 Fragmentation and porosity

Although the HERMES model [17] is capable of describing the development of ignition in HEVR, and DDT, and SDT in pre-damaged, porous beds, the development of porosity and fragmentation is rudimentary. The fracture model of Zywich [18], which is

incorporated in HERMES, applies to discrete fractures. We wish, instead, to develop a spall/fragmentation cloud without specifying individual fractures or fragments. We view this as comprising two separate submodels. The fragment size will be developed as an extension to the fragmentation model in HERMES, which we calibrated to shotgun tests that do not produce ignition. In those tests, fragmentation develops without substantial tensile stress. In the gap tests and fragment impact tests, fragmentation will develop from both tension and compression.

The porosity of a fragmentation cloud increases when velocity gradients cause the volume to increase beyond the strain that corresponds to the tensile strength and/or fracture strain. We will implement failure in a similar spirit as given in [18]. After the fracture criterion is exceeded, the magnitude of the stress (simplified to only consideration of the mean stress) is reduced gradually, reaching zero at a specified failure strain increment. That failure strain of an element is chosen so that fracturing an element of any size absorbs the same energy per unit area. In this way, calculations of tensile failure are relatively independent of mesh refinement, provided that there is adequate resolution. In contrast, a sudden reduction of the tensile stress to zero (such as occurs with simple spall models) results in a significant and unwanted dependence of the fracture and fracture localization on mesh refinement. During the gradual reduction in strength of our method, a portion of the tensile strain is allocated to porosity. After complete failure, all of the tensile strain is allocated to porosity. Subsequent recompaction is aware of the porosity that has been generated. If we assume that the fragments randomly reorder, as a result of rotations introduced during the fracture process, then recompaction meets with resistance at all porosities less than a specified input value (near 50%) that demarks the volume at which there is no longer any edge contact between fragments.

In HERMES, the material strength, and the porosity increase and decrease, (densification) reside in the model for the skeleton of solid material (matrix), not in the solid or gas phases. We propose to develop and test fragmentation and porosity generation as a separate, stand-alone user material for LS-DYNA and ALE3D. The ultimate goal is to demonstrate a validated model. In the absence of data, we seek in the short term to develop a model in which the values of input parameters affect the resulting porosity and fragment size. The parameter values producing a given fragmentation and porosity must be relatively insensitive to mesh refinement. This requirement, if met, will result in a model that can be validated. Once developed, the model can be incorporated into HERMES, and so coupled to ignition and post-ignition behaviour.

1.4.2 Strength of the fragment cloud

The present strength model in HERMES includes damage softening as a result of porosity. We will update that measure of porosity so that damaged material exhibits the pressure dependent strength of porous, granular material. In general, granular materials approach a porosity limit from both higher and lower porosity when sheared. Relatively dense materials dilate, and relatively light materials densify. This porosity limit increases as the normal compressive stress on the plane of maximum shear decreases. We do not plan to incorporate this phenomenon at this time.

1.4.3 Ignition criterion

The ignition criterion in HERMES does not, at present, distinguish fragmented material from solid material. If the combination of shear strain and normal stress is the same, ignition will occur whether the material is fragmented or not. This is not to suggest that, for example, the critical velocity in a Steven test is the same for intact and porous material. Their different compaction and strength properties will lead to different values of the ignition parameter at the same velocity. We do not know whether the parameter will reach the same critical value at the experimental threshold velocity.

1.4.4 Detonation model

When applied to a broad spectrum of porosities, the CREST detonation parameters fitted to a given porosity predict that increased porosity samples are more shock sensitive than measured [19]. The data sets for shock sensitivity over a broad range of porosities are sparse. SDT measured in wedge tests on Tetryl were performed [20] for porosities ranging from 2% to 25%. SDT measured in wedge tests on PETN were performed [21] for porosities ranging from 2% to 21% and also 44% [22]. It is probable that there is more than a single mechanism for ignition in SDT, and that changing the porosity over a substantial range changes the relative importance of the two (or more) mechanisms. Previous studies with CREST over a limited range of porosities (2% to 10% or so) had shown that a single set of CREST parameters was adequate. We can only speculate on the mechanisms that may be at play.

1.4.5 Plan and schedule as of August 2014

Plan, develop, implement and test the stand-alone model for fragmentation and porosity development. Plan and implement the phase 0 modification to CREST detonation model. Prepare interim report. To be completed November 2014.

Plan, develop, implement and test the fragmentation and porosity model integrated with HERMES. Plan and implement the phase 1 modification to CREST. To be completed June 2015

Assess model deficiencies and needs. Identify additional testing needed. Prepare end of year report. To be completed September 2015.

1.4.6 Status as of November 2014

We have implemented and tested the stand-alone model as described below in Section 2. We implemented a phase 0 modification to CREST, to increase the range of porosity for which a given set of parameters would be valid. It was unsuccessful, as discussed in Section 4, where a plan for phase 1 is presented.

2. Fragmentation and fragment cloud formation stand-alone model version 04

2.1 Introduction

The principal feature of XDT is that fragments are formed in a (near) normally dense explosive or propellant, the fragment cloud develops porosity, fragments are subsequently ignited, and the ignition transits to a detonation in the broken, porous material. The first step in implementing this capability in HERMES is to develop a model

for fragmentation and the growth of porosity. We document here the rationale for choices made in developing the initial model, v04.

2.2 Fragmentation

We wished to retain features of the fragmentation model originally developed for PERMS [23] to describe the impact fragmentation that would result from solid rocket motor fallback accidents. In its original form, the specific surface area, *S/V*, was given by

$$\frac{S}{V} = A(\varepsilon - \varepsilon_0)\left\langle \dot{\varepsilon} \right\rangle \tag{1}$$

where ε is the plastic strain, $\left\langle \dot{\varepsilon} \right\rangle$ is the average strain rate, and A and ε_0 are parameters.

For this work we have introduced an input parameter S_{max}, so that the specific surface area is limited to that corresponding to a minimum fragment size, comparable to the explosive crystals. Until the plastic strain reaches the value ε_0, the specific surface area does not change. The use of the average strain rate was to permit extrapolation to linear scale factors spanning several orders of magnitude, and in such a way that geometrically scaled experiments produced the same number of fragments. For our purposes, the test experiments and the system-scale events to which the model will be applied do not differ by such a wide margin. As a result, we simplify the model by eliminating the strain-rate dependence.

In contrast to the fallback application, however, the tests for which the model will be applied includes both compressive and tensile loading. For that purpose, we have chosen to make ε_0 be smaller when the loading is largely tensile, and larger when the loading is compressive. We use the functional form we found suitable for describing ductile failure in metals [24]:

$$d_p = \int_0^{\varepsilon} w_p w_s \, d\varepsilon \tag{2}$$

where the weighting function for shear, w_s, is taken to be unity, and the weighting function for pressure, w_p, is

$$w_p = \frac{1}{1 + p / p_0} \tag{3}$$

where the pressure, p, is positive in compression. As pressure approaches the negative of the input parameter p_0, the weighting function increases without bound. The parameter ε_0 is taken to be the value of plastic strain when the plastic damage variable, d_p reaches a critical input parameter value.

2.3 Porosity increase

In our model, the porosity increases by fracture strain. To accomplish this, we introduce a tensile pressure limit, σ_{t0}, which is given by

$$\sigma_{t0} = \sigma_0 \left(1 - \frac{\alpha_{mx} - 1}{\alpha_f - 1}\right) \exp\left(-\frac{S}{V} L_0\right) \tag{4}$$

so long as an element's maximum value of Herrmann's α parameter, α_{mx}, is less than the input parameter value of α at failure, α_f. Volume expansions larger than α_f support no tensile stress. Here σ_0 and L_0 are input parameters. The reduction of the tensile pressure limit with fragment size (via S/V) is a way to account for the reduced ligament area of binder as the fragments get smaller.

If the tensile pressure is calculated to be less than the tensile pressure limit, the value of the tensile pressure is reduced, and some of the volume strain is taken up as porosity. This is done in a gradual way, rather than suddenly reduced to zero, following the method of tensile fracture described by Zywich [18]. We record the value of α_l when the tensile pressure first exceeds the limit. We describe a damage value, D, which starts at zero, and increases to 1 when α increases from α_l to $\alpha_l + \varepsilon_f$. The input parameter ε_f is set so that creating a fracture surface with the same area requires the same energy, independent of the mesh size, Δx. For 3D calculations with a fixed σ_{t0}, this requires $\varepsilon_f \sim 1/(\Delta x)$. Following Zywich, we also assume it to be the case for 2D axisymmetric calculations as well.

In our simplified model, we use only the tensile pressure, so that we can solve for the new damage, D, α, and porosity without iteration if the calculated tensile pressure exceeds $\sigma_{t0}(1-D)$.

$$
\begin{aligned}
\varepsilon_t &= \frac{\sigma_{t0}}{K} \\
D &= \frac{1-\varepsilon_t-\alpha_l/V}{\varepsilon_f/V-\varepsilon_t} \\
\alpha &= \alpha_l + D\varepsilon_f \\
p &= -\sigma_{t0}(1-D) \\
\varphi &= 1-1/\alpha
\end{aligned}
\tag{5}
$$

where φ is porosity, V is the relative volume, K is the bulk modulus of the solid, and following Herrmann, the equation of state of the distended solid is $f_s(\alpha/V)$ where the function $f_s(1/V)$ is the equation of state of the solid. In our implementation, we simplify the equation of state to be

$$
p = K\left(\frac{\alpha}{V}-1\right) \tag{6}
$$

Once the variable D reaches 1, or the relative volume exceeds α_f, the tensile pressure is never permitted to exceed zero. If the tensile pressure is calculated to exceed zero, then all the expansion from zero pressure is taken up as porosity, and α takes the value V.

2.4 Strength

The element strength,Y, for this model is calculated by interpolation between the intact and broken parameter set

$$Y = \min\left(Y_{\max}, Y_a + Y_b p\right)(1-D)$$

$$Y_a = Y_{ai} + \left(Y_{af} - Y_{ai}\right)\frac{\alpha_{mx} - 1}{\alpha_f - 1} \tag{7}$$

$$Y_b = Y_{bi} + \left(Y_{bf} - Y_{bi}\right)\frac{\alpha_{mx} - 1}{\alpha_f - 1}$$

where the Y_a and Y_b subscripts *i* and *f* refer to intact and broken. In those cases where the relative volume is less than the failure value α_f, the compressive pressure is limited by a crush curve.

$$P_c = f_p Y_a + \left(P_{cr0} - f_p Y_a\right)\left(1 - \frac{\alpha - 1}{\alpha_{mx} - 1}\right) \tag{8}$$

where f_p, P_{cr0}, and *r* are parameters. For relative volume that corresponds to an excess compression greater than μ_{cr}, defined as P_{cr0}/K, the solid equation of state is used and α takes the value 1.

2.5 Fragment size *vis-à-vis* mesh size

In these calculations, we do not seek to identify individual fragments comprising blocks of contiguous elements. Instead, we are striving for a continuum representation. If the specific surface area implies a fragment size larger than the element volume, we interpret that element to contain a portion of a larger fragment. In tallying the fragment size distribution, we count that element's contribution as an appropriate fraction of a particle. If the fragment size is less than the element volume, then we count that element to contain multiple fragments, but not necessarily an integer number.

2.6 Implementation of stand-alone model

This model has been implemented as an LS-DYNA user material. The 15 history variables in the present version (04) are identified in Table 1.

Table 1. History variables and their description

Index	Symbol	Description
1	V	Matrix relative volume
2	α	Current value of Herrmann's parameter
3	ϕ	Current value of porosity, 1 - 1/α
4	α_{mx}	Maximum α experienced for this element
5	σ_t	Maximum tensile stress for this element, σ_{t0}(1-D)
6	f	Mass fraction of gas (not changed in this implementation)
7	μ_{cr}	Excess compression at complete crush
8	p	Pressure
9	Y	Yield strength
10	ε_0	Plastic strain below which surface area is not produced, Eq. 1
11	d_p	Augmented strain integral, Eq. 2

12	α_t	Value of α where strength is zero, $\alpha_l + \varepsilon_f$
13	S/V	Specific surface area
14	D	Fracture parameter
15		not used

There are 28 input parameters for version v04. They are identified in Table 2.

Table 2. Input variables and their description

Index	Symbol	Description
1	if3d	0 for 2-D, 1 for 3-D simulation
2	ptol	Relative tolerance for iteration
3	K	Bulk modulus
4	G	Shear modulus
5	ρ_{0m}	Reference density of solid
6	ρ_{0g}	Reference density of gas
7	α_f	Value of α above which all cohesion and strength is lost
8	P_{cr0}	Maximum crush pressure, Eq. 8
9	r	Power in crush curve, Eq. 8
10	ϕ_i	Initial porosity
11	σ_0	Maximum tensile strength, Eq. 4
12	Δx	Nominal mesh size (not used)
13	$\mathcal{G}$	Energy release rate related to fracture toughness (not used)
14	ε_f	Incremental volume strain over which strength reduces to 0, Eq. 5
15	Y_{ai}	Intact strength offset, Eq. 7
16	Y_{bi}	Intact strength pressure dependence, Eq. 7
17	Y_{af}	Failed strength offset, Eq. 7
18	Y_{bf}	Failed strength pressure dependence, Eq. 7
19	Y_{max}	Maximum yield strength, Eq. 7
20	d_{p0}	Augmented strain integral critical value
21	A	Fragmentation parameter, Eq. 1
22	p_0	Augmented strain integral parameter for w_p, Eq. 3
23	w_{s0}	Augmented strain integral parameter for w_s (Not used, $w_s = 1$)
24	L_0	Characteristic fragment size to affect tensile strength, Eq. 4
25	f_p	Factor for calculating minimum crush strength, Eq. 8
26	S_{max}	Maximum specific surface area, Eq. 1
27	e_{fail}	Plastic strain above which element is deleted from calculation
28	V_{fail}	Relative volume above which element is deleted from calculation

2.7 Application of the stand-alone model

2.7.1 Sphere impacting a plate

The sphere impacting a plate is a simplification of the BVR geometry used by Finnegan [8]. In our test case a 10-mm diameter steel sphere at 300 m/s impacts a 100-mm diameter by 10 mm thick plate. When brittle fracture is suppressed, the steel sphere

pushes out a bubble of material that continues to thin as the sphere moves beyond the back of the plate. See Figure 1. In contrast, when brittle fracture is permitted, the plate fractures. In the continuum representation, the broken plate expands as a relatively thick shell of fragments. See Figures 2 and 3 for the appearance of the fracture pattern when the mesh size is varied by a factor of 2. The model parameters for these simulations are given in Appendix B.

Our intent for these simulations was to demonstrate a model that would incorporate the extremes of behaviour under fragment attack. The design of the model is such that the fragment size is independently specified. In this way, a cloud of fragments can contain small particles, so upon ignition would burn relatively rapidly, or large particles, which would burn slowly. The more the cloud expands, the sparser the cloud becomes, so that the gas products expand and cool to a reduced pressure. The gas also has farther to travel to ignite other particles. Both of those factors may contribute to a reduced pressure build-up and possibly extinction of the burn.

2.7.2 Pointed projectile impacting a plate

We show a much thicker slab of material 140 mm diameter by 70 mm thick being attacked by an 8 mm diameter 25 mm long, conically tipped projectile at 900 m/s. With brittle fracture permitted, a cloud of fragments is produced at the rear of the plate, in general agreement with the experimental observations of Cook [10]. (See Figure 4.) This calculation is flawed. The projectile nose has penetrated through several elements of the target without directly pushing them aside. We attempted to permit the elements to break away from the symmetry axis under radial tension, but the stresses near the projectile nose are compressive, so the attempt was for naught. We will incorporate the model in ALE-3D and repeat both impact calculations using either ALE or Eulerian simulations.

3. DDT Simulations

3.1 Introduction

As a result of the successful application of post-advection fix-up in ALE-3D, we have been able to perform DDT simulations in an ALE or Eulerian framework. This has permitted successful simulations to late times. We report here some recent applications of DDT using Lagrange simulations.

3.2 Simulations of DDT in LX-04 molding powder beads

We refined the DDT studies reported in [25] to include new information about the measured particle size distribution. That size distribution was reasonably well represented as a log normal distribution centered at 2.3 mm with a corresponding R value of 1.4. (See Appendix A.) We calculated the deflagration to detonation transition for 15% porous material, at which porosity we had the SDT measurements of Garcia [26] for HMX powder. The calculations of [25] place the powder in a 25 mm ID, 75 mm OD steel tube that is 340 mm long. When we used parameters that correspond to the measured particle size distribution, our calculated transition to detonation was at 140 mm from the ignition plane. Tests performed at 10 and 30% porosity showed transition at 200 and 110 mm respectively. No tests were performed at 15% porosity. These results were reported in [17].

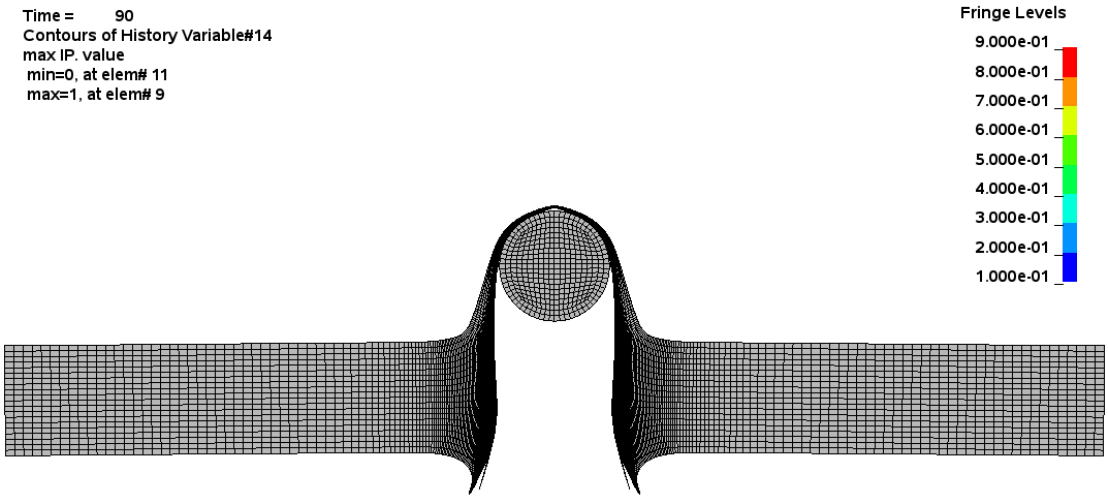

Figure 1. Simulation of 10 mm steel sphere into 10 mm thick plate at 300 m/s. The plate model has had tensile fracture suppressed by the choice of input parameters. The fringe plot is of the damage variable D.

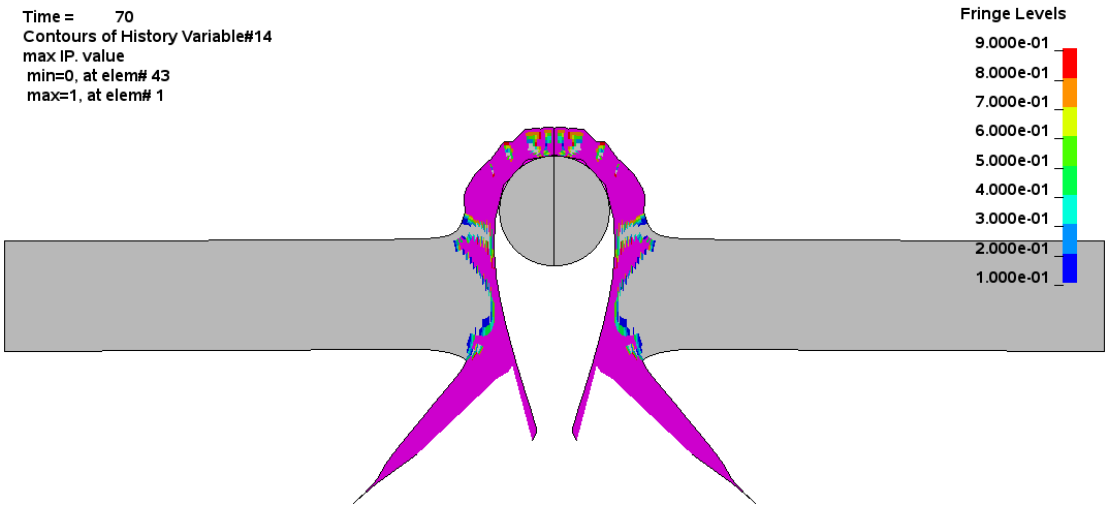

Figure 2. Simulation of 10 mm steel sphere into 10 mm thick plate at 300 m/s, using same plate mesh as in Figure 1. The plate model permits tensile fracture by the choice of input parameters.

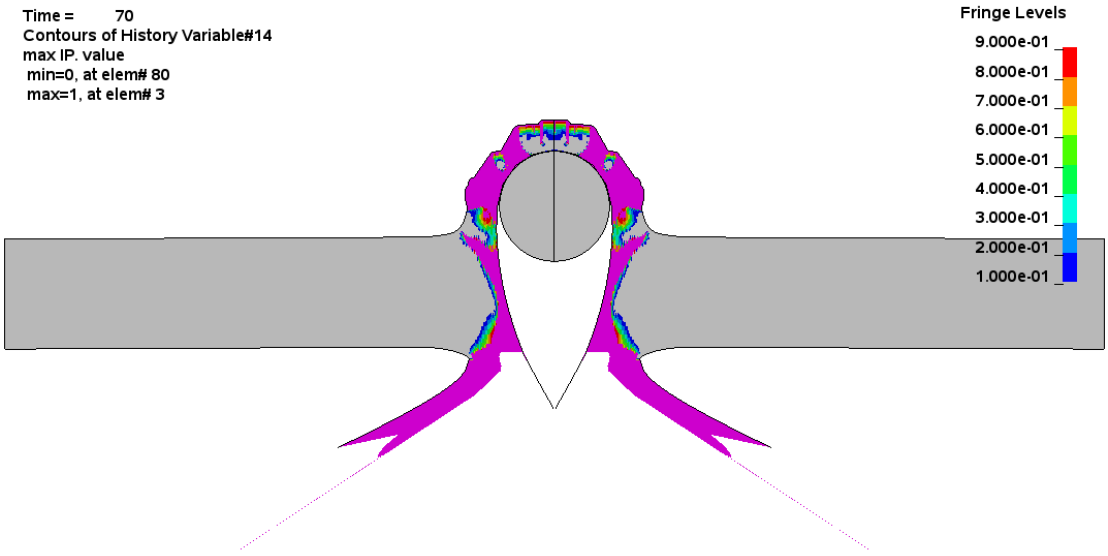

Figure 3. Simulation of 10 mm steel sphere into 10 mm thick plate at 300 m/s. Plate has same tensile properties as in Figure 2, but the mesh size has been decreased by a factor of 2 and ε_f is doubled. The fracture pattern is nearly stationary.

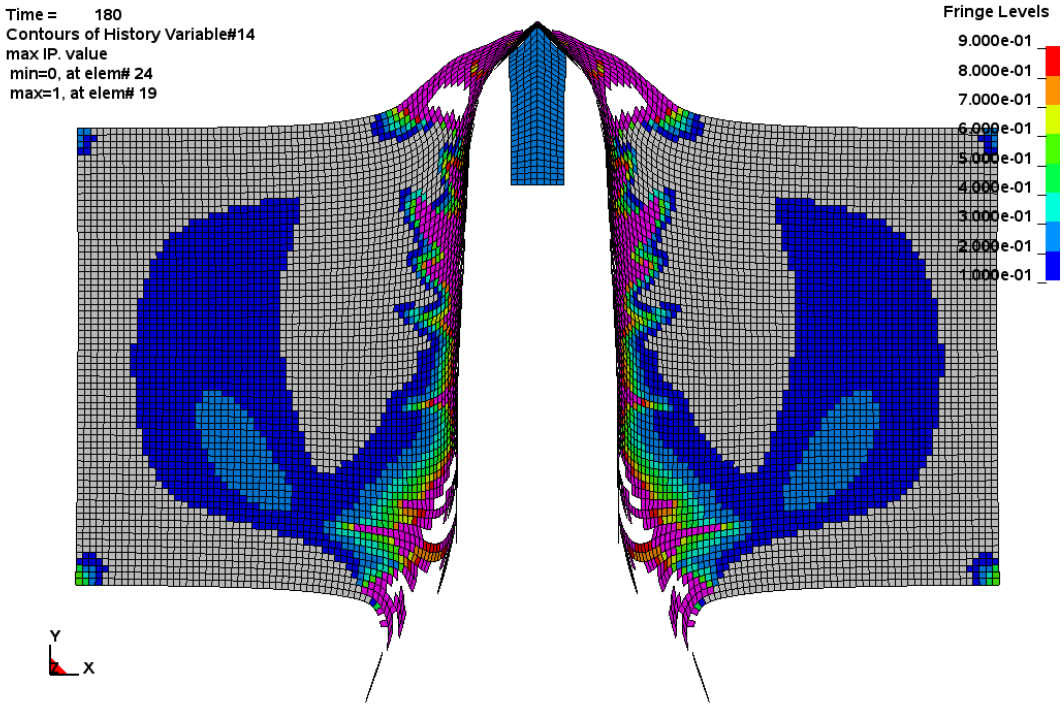

Figure 4. Simulation of a conical-nosed steel projectile 8 mm diameter into a 70 mm thick plate at 900 m/s. The cloud of fragments separates from the plate.

3.3 Simulations of DDT in PETN powder

Luebcke [27] reported results on 180-micron PETN powder in his much smaller apparatus (5 mm ID, 25 mm OD steel cylinder, 44 mm long) than the one used in [25]. We had fitted CREST-lite parameters [19] to SDT data [21] at density 1.4, which corresponds to 22% porosity. Simulations [28] using those parameters in Luebcke's geometry did not produce DDT. Instead, the porous powder only burned to completion after being reached by the ignition front that spread from the ignition plane, so would have resulted in a relatively benign pressure burst.

Closer inspection of those results showed that the burn fraction in the tube was starting to increase with the CREST logic as the pressure built to a relatively low-amplitude shock. The simplified equation set is shown below.

$$
\begin{aligned}
B_1 &= C_0 Z^{C_1} \\
B_2 &= C_2 Z^{C_3} \\
M_1 &= C_6 (1-\lambda) / B_1^{1/2} \\
M_2 &= (C_8 Z^{-C_9} + C_{10} Z^{C_{11}})(1-\lambda) / B_2^{1/2} \\
\dot{\lambda}_1 &= (1-\lambda_1)\sqrt{-2B_1 \ln(1-\lambda_1)} \\
\dot{\lambda}_2 &= \lambda_1 (1-\lambda_2)\sqrt{2B_2\left[B_2\lambda_1 / B_1 - \ln(1-\lambda_2)\right]} \\
\dot{\lambda} &= M_2 \dot{\lambda}_2
\end{aligned}
\tag{9}
$$

Here the notation is the same as [29]. In HERMES, the simplifications $C_6 = 0$ and $C_8 = 0$ are taken. With these simplifications, the parameter M_2 has the simple form

$$
M_2 = \frac{C_{10}}{\sqrt{C_2}} Z^{C_{11} - C_3/2} \tag{10}
$$

If the parameter C_{11} is too large relative to C_3, then the value M_2 can be less than 1 for reasonable values of the entropy function Z. If that happens then the mass fraction of gas gets stuck at some intermediate value, since after λ_2 reaches the value 1 the changes in λ_2 and λ are henceforth zero according to the CREST equations.

This was happening in our simulations. The method used by HERMES is to calculate the change in the burn fraction λ from both the CREST logic and the HEVR logic by which particles are burned from their surfaces. As a result, the burn completed, but only on the much longer time scale for the ignition front to propagate through the explosive bed.

We refitted the CREST-lite parameters, but with the constraint

$$
C_{11} = 0.2 + C_3 / 2 \tag{11}
$$

The fit to the SDT data at density 1.4 was equivalent to the previous fit, but with this set, we achieved transition to detonation at a position 22 mm from the ignition plane. The experiments with densities between 1.39 and 1.41 showed detonation transitions between 18 and 25 mm.

We performed two additional simulations of DDT. The Luebcke apparatus has a 5 mm ID and 25 mm OD. We modified the inner diameter of the apparatus, and kept the outer diameter fixed. We anticipated that a reduced inner diameter would have more confinement, and so reduce the transition distance. Instead, the result for 2 mm ID was a transition at 24 mm, and 8 mm ID was a transition at 20 mm. We observed that the pressure history at the same axial locations upstream from the transition had reduced pressure in the 2 mm ID compared with the 5 mm and 8 mm ID geometries. Although the wall was thicker, plastic deformation in the tube wall near the ID was increasing the volume in the small ID case, and so more effective at reducing the pressure.

4. Unresolved Issues with HERMES as of November 2014

4.1 Increase in matrix stress when burning

We developed a one-element calculation with fixed boundaries, so that the volume does not change, and designated that element to be ignited at time zero. The element size (10 mm on a side) and fragment size (1 mm) are such that the burn completes in 200 μsec. With the present logic, the matrix stress starts at zero, but then increases (and eventually decreases to zero) during the burning. Since the matrix specific volume, v_m, is given by

$$v_m = \frac{v}{1-\lambda} \tag{12}$$

where v is the specific volume of the element, which doesn't change by virtue of the rigid boundaries, and λ is the mass fraction of gas. As a result, the matrix specific volume is always increasing, so the adiabatic and matrix energy densities always decrease to a relatively large negative value.

It is unlikely that this is the correct answer, but it is unclear what the correct answer should be. In the limit of slow, subsonic burning it seems more plausible that the matrix stress would not change. It is possible that a mesoscale simulation, using the ALE-3D capability of initializing and growing a burn front may be useful here. Previous simulations of a mesoscopic calculation of the stresses in the unburned material surrounding a constellation of hot spots have been difficult to unravel. The stress field is both time- and space-dependent. Perhaps by recording the solid energy density change, gas pressure, and matrix specific volume, we can infer what the consistent macroscopic matrix stress must be by differentiation of the smoothly changing internal energy density.

4.2 Weak shock in a non-reacting, porous explosive

Driving a weak shock into a non-reacting explosive (by setting the particle diameter input as zero, so no burning from surfaces, and the threshold value of Z to a large value, so no CREST burning either) results in a negative adiabatic energy density in the elastic-precursor. It is small, but should not be negative. A preliminary examination suggests that the adiabatic energy of the solid is incorrectly calculating a correction that involves adiabatic energy of the matrix.

4.3 Differences in SDT results between HERMES/LS-DYNA and PERUSE

Calculations of SDT performed by Maheswaran with PERUSE [19] and with HERMES in LS-DYNA have significantly different run distances in porous PETN for the same shock input. Calculations by Curtis [28] with non-reacting PETN have shown that the Z parameters in the two calculations are the same for the same shock input. Earlier calculations to obtain the reaction history for a constant value of Z using the PERUSE and LS-DYNA subroutines have resulted in the same reaction rate for the same Z value. Those latter calculations were performed some time ago, with a much earlier version of HERMES. We recommend that they be repeated using a simple driver on the actual subroutines used in current versions of PERUSE and of HERMES. If driver calculations at the same Z value give different reaction histories, then those differences must be traced and corrected. If, instead, they give the same reaction history, then the differences must lie in the calculation of Z for partially burned explosive. Note that this observation may be related to the observation in Section 4.1 above. As a result, the issue should be pursued in cases where the matrix strength is present, and also where it is set to zero by input.

4.4 CREST parameters do not fit broad ranges of density variation

Maheswaran [19] reported that a single set of CREST parameters did not simultaneously fit the PETN density at 1.0, 1.4, and 1.7 g/cc. As discussed in Section 1.4.4, we found this to be true for other explosives over a broad range of porosity. As Lambourn [30] has noted, the hydrodynamic effect of porosity is to increase the entropy factor at a given shock strength, but also to increase the ease with which pressure increases can catch up to the shock front (catch-up factor) and thereby increase the shock strength. Both of these factors would tend to increase the shock sensitivity with porosity. What we observe instead is that a set of parameters fitted to one density overestimates the shock sensitivity at lower density. We had proposed that a modification that scaled back the entropy with increasing porosity might suffice. We found that inadequate because the catch-up factor is also a function of shock strength.

Although it would be convenient to have a single set of parameters for all porosities, calculations from a given initial porosity (for example DDT simulations) could be performed even if the different initial porosities were considered to be unique materials. For application to XDT, however, the situation is more critical. The feature of XDT is that porosity evolves, and the response has been observed to be different when the expanding cloud intercepts a plate at different distances, and so different porosities.

We suggest the following procedure as an approach to scaling the entropy parameter with porosity. Fit the CREST parameters to the shock sensitivity measured at an intermediate porosity. With the same set of parameters, calculate the run distance at a different porosity as a function of the entropy parameter, Z. From that curve, calculate the value of Z needed to achieve the desired run distance at a given shock strength. From the values of Z as a function of shock strength, calculate the necessary Z-multiplier. Fit a curve to the Z-multiplier as a function of the calculated value of Z. Repeat for other porosities. Interpolate for intermediate values of porosity.

We tentatively interpret the failure of a single set of CREST parameters to work over a broad range of porosity with reference to the mesoscale. The build-up of reaction in heterogeneous explosives is dominated by the inhomogeneous hot spots produced, which comprise the tail of the distribution of mass exceeding a given temperature. With increasing porosity, we hypothesize that the tail of the distribution changes, in accord with the changing localization. At small porosity, the hot spots arise from the collapse of a constellation of holes. At large porosity, we hypothesize that the hot spots arise from an assembly of grains shearing on the surface as they try to fill nearby holes. We perhaps should not expect the same relation between a continuum variable such as Z and the tail of the different distributions that arise in the extreme cases.

5. Acknowledgements

Interactions with Hugh James and Malcolm Cook at AWE have significantly increased my understanding of the varieties of XDT, and stimulated my thinking on requirements of a model and how a model might be developed. It is a pleasure to acknowledge their willingness to share information and thoughts about this topic.

6. References

1. Robert L. Keefe, "Delayed Detonation in Card Gap Tests," *Proc. 7th Symp. (International) on Detonation*, June 1981, Annapolis, MD, p265.
2. R. C. Jensen, E. J. Blommer, and B. Brown, "An Instrumented Shotgun Facility to Study Impact Initiated Explosive Reactions," *Proc. 7th Symp. (International) on Detonation*, June 1981, Annapolis, MD, p301.
3. L. G. Green, E. James, E. L. Lee, E. S. Chambers, C. M. Tarver, C. Westmoreland, A. M. Weston, and B. Brown, "Delayed Detonation in Propellants from Low Velocity Impact," *Proc. 7th Symp. (International) on Detonation*, June 1981, Annapolis, MD, p256.
4. L. Green, E. James, and E. Lee, "Energetic Response of Propellants to High Velocity Impacts," *Proc. 8th Symp. (International) on Detonation*, July 1985, Albuquerque, NM, p284.
5. B. Salvetat and J. F. Guery, "Visualization and Modelling of Delayed Detonation in the Card Gap Test," *Proc. 10th International Detonation Symp.*, July 1993, Boston MA, p709.
6. R. R. Bernecker, A. R. Clairmont, Jr., and L. C. Hudson, III, "Prompt and Delayed Detonation from Two-Dimensional Shock Loadings," *Proc. 10th International Detonation Symp.*, July 1993, Boston MA, p476.
7. Yves Guengant and Michel Quidot, "Experimental and Numerical Study of XDT Using the Double Card Gap Test," *Proc. 11th International Detonation Symp.*, August 1998, Snowmass, CO, p701.
8. S. A. Finnegan, A. I. Atwood, J. K. Pringle, N. G. Zwierzchowski, P. O. Curran, and J. Wiknich, "The Application of Ballistic Impact and Radiant Ignition Techniques for Characterization of Violent Reaction in Cased Propellant," *Proc. 10th International Detonation Symp.*, July 1993, Boston MA, p320.
9. P. J. Haskins, M. D. Cook, and P. J. Cheese, "An Investigation of XDT Events in the Projectile Impact of Secondary Explosives," *Proc. 10th International Detonation Symp.*, July 1993, Boston MA, p148.

10. Malcolm D. Cook, Peter J. Haskins, Richard I. Briggs, Helen Flower, Phillip Ottley, Andrew D. Wood, and Phil J. Cheese, "An Investigation into the Mechanisms Responsible for Delayed Detonations in Projectile Impact Experiments, *Proc. 13th International Detonation Symp.*, July 2006, Norfolk, VA, p814.
11. P. J. Haskins, M. D. Cook, and P. J. Cheese, "Studies of XDT Phenomena under Fragment Attack Impact Conditions," *Sci. Tech. Energetic Materials*, **66**, 5, 2005.
12. Peter J. Haskins, Richard I Briggs, and David W. Leeming, "Dual Fragment Impact," *Proc. 15th International Detonation Symp.*, July 2014, San Francisco, CA, (in publication)
13. A. S. Dyer, P. J. Hubbard, P. R. Lee, and D. G. Risley, "Factors Affecting the Explosiveness of Munition Fillings," *Proc. 7th Symp. (International) on Detonation*, June 1981, Annapolis, MD, p1040.
14. M. D. Cook, A. D. Wood, P. R. Ottley, and P. J. Cheese, "Observation of sub-detonation resonse in confined high density HMX based PBXs," *Proceedings of the APS-SCCM and AIRAPT-24 Joint Conference*, Seattle WA, July 2013, Journal of Physics: Conference series 500 2014.
15. B. Stokes, A. Sanderson, and P. Kernen, compilers, "Cookoff and XDT Mechanisms," NIMIC report NIMIC-S-172-96 Volume II, April 1997.
16. Malcolm Cook, private communication, AWE, August 2014.
17. J. E. Reaugh, J. P. Curtis, and M.-A. Maheswaran, "Computer Simulations to Study the Effects of Explosive Energetic and Constitutive Properties on the Deflagration to Detonation Transition," *Proc. 15th International Detonation Symp.*, July 2014, San Francisco, CA, (in publication)
18. E. Zywich, private communications, LLNL, summer and fall 2013. Also see DYNA3D user manual, LLNL, 2007 and later.
19. Mary-Ann Maheswaran, John P. Curtis, and John E. Reaugh, "Modelling the shock to detonation transition in PETN using CREST," *Proc. 15th International Detonation Symp.*, July 2014, San Francisco, CA, (in publication)
20. I. E. Lindstrom, *J. Appl. Physics*, **41** (1) p337, 1970.
21. Terry R. Gibbs and Alphonse Popolato, eds., *LASL Explosive Property Data*, University of California Press, Berkeley, CA, 1980, p315-319.
22. G. E. Seay, L. B. Seely, "Initiation of Low Density PETN Pressing by a Plane Shock Wave," *J. Appl. Physics*, **32**, p1092, 1961.
23. J. L. Maienschein, J. E. Reaugh, and E. L. Lee, *Propellant Impact Risk Assessment Team Report: PERMS Model to Describe Propellant Energetic Response to Mechanical Stimuli*, UCRL-ID-130077, February 27, 1998.
24. M. L. Wilkins, R. D. Streit, and J. E. Reaugh, "Cumulative-Strain-Damage Model of Ductile Fracture: Simulation and Prediction of Engineering Fracture Tests," UCRL-53058, October, 1980.
25. Reaugh, J.E., Curtis, J.P., and Maheswaran, M-A, "Computer Simulations to Study the Effects of Explosive and Confinement Properties on the Deflagration to Detonation Transition (DDT)," *Proceedings of the APS-SCCM and AIRAPT-24 Joint Conference*, Seattle WA, 2013, available as LLNL report, LLNL-PROC-656113.
26. Garcia, F., Vandersall, K.S., and Tarver, C., "Shock Initiation Experiments with Ignition and Growth Modeling on Low Density HMX," *Proceedings of the APS-SCCM*

and AIRAPT-24 Joint Conference, Seattle WA, July 2013, Journal of Physics: Conference series 500 2014.
27. P. E. Luebcke, P. M. Dickson, J. E. Field, "Deflagration-to-Detonation Transition in Granular Pentaerythritol Tetranitrate, *J. Appl. Phys.* **79** p3499, 1996.
28. J. P. Curtis, "Modelling Shock to Detonation Transition and Deflagration to Detonation Transition in PETN using LS-Dyna with HERMES V77e," AWE technical memorandum AWE/EDMS3/8021/15A84, August 2014.
29. C. A. Handley, "The CREST Reactive Burn Model," *Proc. 13th Intl. Detonation Symposium*, Norfolk, VA, July 2006, p864.
30. B. D. Lambourn, "An Improved EOS for Non-Reacted Explosives," AIP Conference Proceedings 845, Baltimore, MD, August 2005, p165.
31. J. E. Reaugh and A. G. Jones, "Mechanical Damage, Ignition, and Burn: Experiment, Model Development, and Computer Simulations to Study High-Explosive Violent Response (HEVR)," *Proc. 14th Intl. Detonation Symposium*, Coeur d'Alene, ID, July 2010, p909.

Appendix A. Log normal distribution

Particle size distributions often follow a lognormal distribution in differential mass as illustrated in Figure A1. For particles of adequate size, physically sifting a representative sample of the material on a stack of sieves, and weighing the material retained on each sieve determines these distributions. If the particles are too small, other methods must be used. The distributions are displayed as the retained mass in a given bin with nominal size, D. I have characterized the lognormal distribution by the mean diameter, D_m and the ratio, R. The two bins centered at RD_m and D_m/R have retained masses equal to half the mass retained on the bin centered at D_m. The range of R values illustrated in Figure A1 encompasses typical monomodal particle size distributions for HE crystals.

The burn of these lognormal distributions is quite well represented by a standard form factor, so that

$$\dot{\lambda} = v(p)\frac{S}{V}\Big)_0 (1-\lambda)^p \tag{A1}$$

where λ is the mass fraction of product, $v(p)$ is the laminar burn speed of the flame front that decreases the radius of the particles, and $\frac{S}{V}\Big)_0$ is the specific surface area of the starting distribution before any burning takes place. The form factor is evaluated by calculating $\dfrac{\dot{\lambda}}{v(p)\frac{S}{V}\Big)_0}$ for the specific distribution under consideration. The results of "burning" the three lognormal particle size distributions are shown as a function of λ by the solid curves in Figure A2. Here "burning" is the numerical integration of the mass change as particles, distributed in up to 200 bins, decrease in size by 0.2% of the median

diameter. The curves are fitted to a form factor $(1-\lambda)^p$ and the fitted curves are also shown in Figure A2 as the thin dashed lines. In general, the fit is better for narrow distributions, but all three distributions are fitted quite well.

The specific surface area for a broad distribution is larger than that of a narrow distribution with the same median diameter, due to the contribution of the fine particles. We evaluated that specific surface area as a function of the distribution width, R, and fitted a curve to those results for the purpose of interpolation. The calculated values and the fitted curve are shown in Figure A3. The curve fit is given by

$$\begin{aligned} D_m \frac{S}{V}\Big)_0 &= 6 + 0.098(R-1) + 1.271(R-1)^2, \quad R \le 1.57 \\ &= 5.7 + 1.152(R-1) + 0.315(R-1)^2, \quad R > 1.57 \end{aligned} \tag{A2}$$

The power, p, in the form factor was determined as individual best fits for several different values of the distribution width, R, and then fitted as a function of R.

$$\begin{aligned} p &= \tfrac{2}{3} + 0.0675(R-1) + 0.427(R-1)^2, \quad R \le 1.48 \\ &= 0.578 + 0.439(R-1) + 0.0228(R-1)^2, \quad R > 1.48 \end{aligned} \tag{A3}$$

The individual best fits of the power, p, for various values of R are shown in Figure A4, together with the fitted curve (Eqs A3).

With these fits, the burn-up of lognormal particle size distributions may be treated as the burn-up of a single equivalent particle, with matched specific surface area, so long as the power, p, is appropriate for the width of the distribution and not the single sphere value of 2/3.

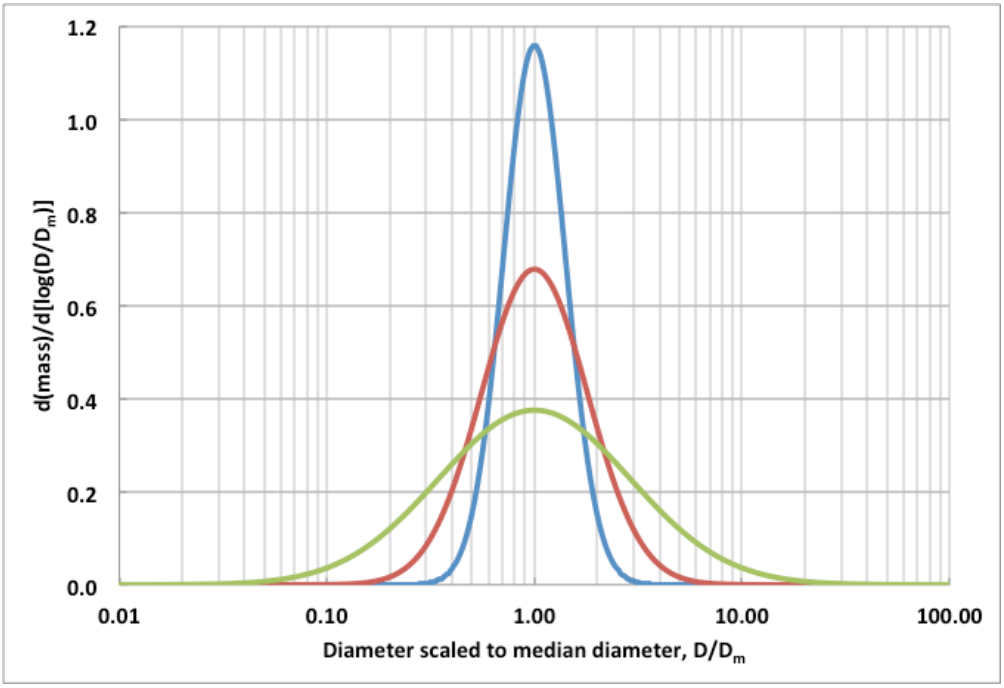

Figure A1. Lognormal distribution of the differential mass per bin width as a function of particle diameter scaled to the median diameter, D_m. The illustrated distributions have R-values of 1.5 (narrowest), 2.0 and 3.5 (widest).

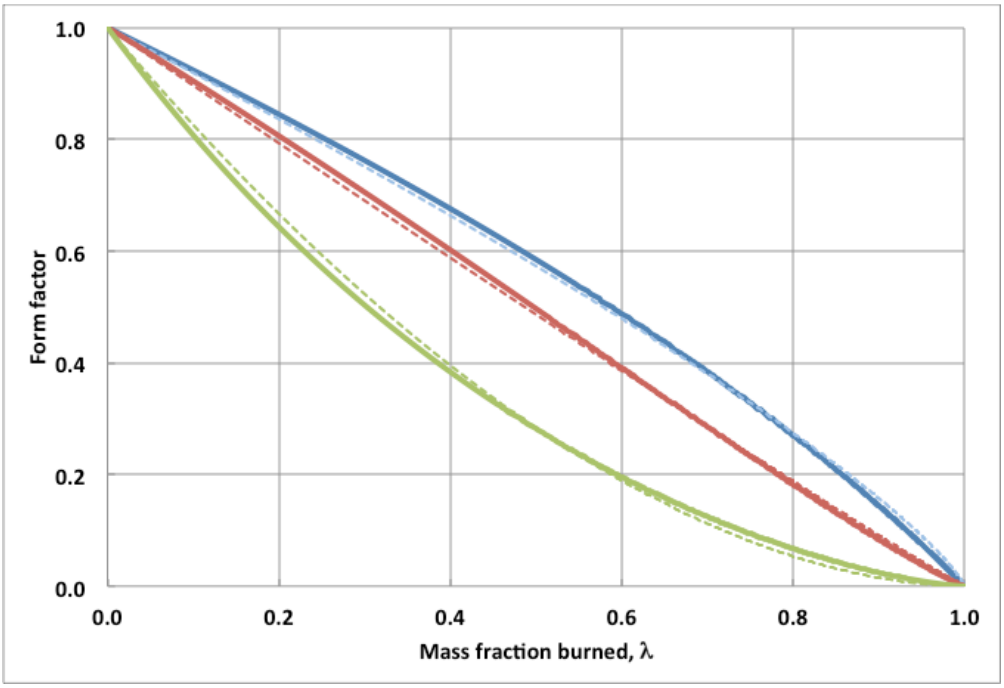

Figure A2. Form factor that controls burn-up of the particle size distribution (Eqs 3) as a function of the extent of reaction, λ, for the three distributions shown in Fig 1. The fitted curves are the dashed lines.

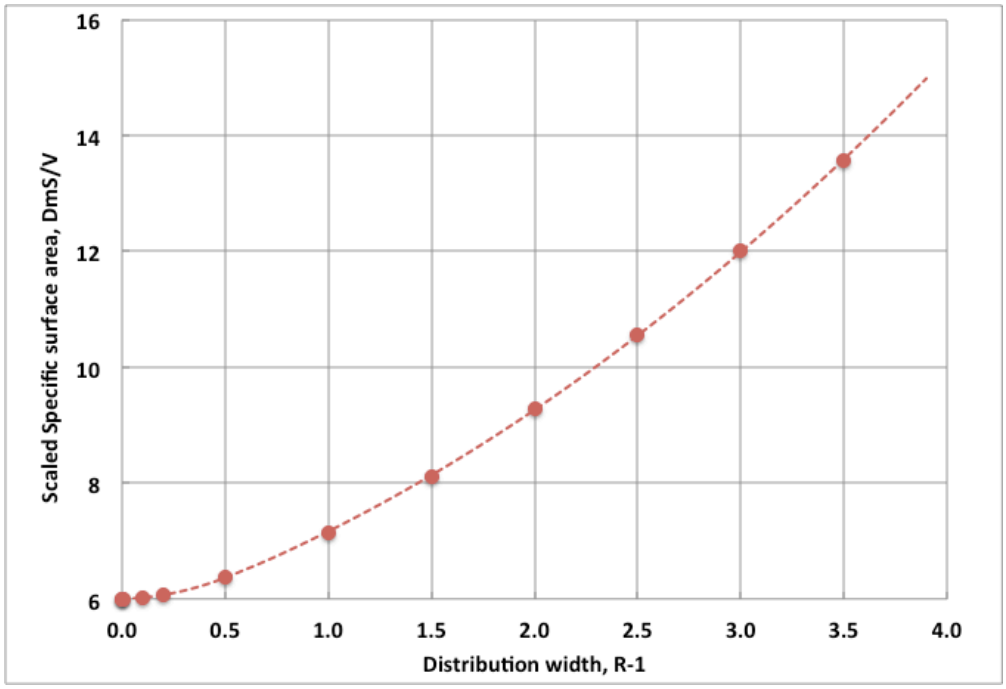

Figure A3. Scaled specific surface area as a function of the distribution width measure, R. The fitted curve is the dashed line.

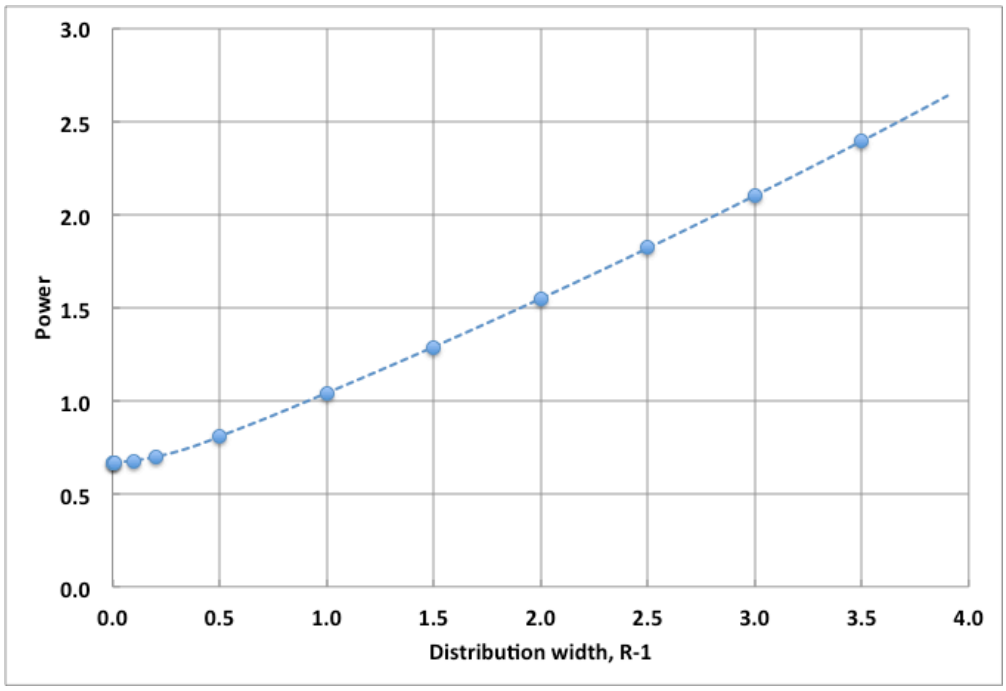

Figure A4. Power, p, as a function of the distribution width measure, R. The fitted curve is the dashed line.

Appendix B. Input parameters for LS-DYNA simulations

B1. Sphere impact on plate (LS-DYNA)

For these calculations, the model was simplified to include a constant yield stress of 0.3 kbar, and the formation of specific surface area was suppressed. Table B1 below includes parameters for the case with brittle fracture. For the case with ductile stretching, the single parameter sigt0 is changed to 0.001 (multiplied by 10). The brittle fracture set was also used for the conical-nosed projectile simulation. For the sphere impact mesh study, the coarser mesh used the value 0.05 for *epsf*.

Table B1. LS-DYNA input for the stand-alone fragmentation model (brittle fracture permitted)

mid	ro	mt	lmc	nhv	iortho	ibulk	ig
1	1.95	48	28	15	0	3	4
ivect	ifail	itherm	ihyper	ieos			
0	1	0	0	0			
if3d	tol	bulk	shear	r0m	r0g	afail	pcr0
0.	1.e-8	0.3	0.1	1.95	0.001	1.395	0.003
oopow	phi0	sigt0	dx0	ggg	epsf	yai	ybi
0.3333	0.03	0.0001	0.1	2.e-9	0.100	0.0003	0.
yaf	ybf	ymax	dp0	A	p0	ws0	L0
0.0003	0.	0.002	0.2	0.	1.	0.	0.
fp	Smax	epsf	vrelf				
0.667	300.	50.	1.4				

B2. LS-DYNA input for HERMES calculation of DDT in porous PETN, density 1.4

These calculations used the new fit to PETN shock to detonation transition. The material input parameters are given in Table B2. (The glossary of input parameters appears in Appendix C.) There are no data for the strength of porous PETN. In the absence of data, we used the parameter values we had fitted to the AWE explosive described in [31]. We reported the effect of strength vs. no strength to be up to a 17% increase in the DDT transition distance.

Table B2. LS-DYNA input for DDT in PETN

mid	ro	mt	lmc	nhv	iortho	ibulk	ig
2	1.4000	47	44	66	0	2	3
ivect	ifail	itherm	ihyper	ieos			
0	0	0	0	0			
if3d	bulk	shear	eps0	epspow	epsA	snorm	normpow
0.	0.35	0.02	0.2	1.	160.	0.0005	0.5
shearpow	Tinit	Tshift	phicr	capD	cres	y0	s0
5.	293.	0.079910	0.00082	930.	1.10	490.e-6	1.00

em0	en	epsh	edot0	edpow	capC	ares	bten
0.44	0.50	0.045	5.6e-6	0.14	0.032	1.2e-5	0.24
capA0	capA1	minp	miny	fail	maxit	tol	tolp
0.	0.51	-1.e-2	0.0	1.	30.	1.e-5	1.e-5
fmc	fib	cmlow	cmhih	cmtau	ystrmx	ifa3d	frsigc
0.0	4.0	0.02	0.02	1.	2.e-3	0.	-1.
frscripg	frdxel	frtol	frsmls				
3.3e-8	0.025	1.e-5	0.333				

In the parameter input file (eos.paramv83) the labels shown below may not appear. They a listed here for convenience. (The glossary for these input parameters appears in Appendix C.) The unreacted equation of state is the one used in [19]. The tabular product equation of state is also described there. The CREST-lite parameters were fitted to the run-to-detonation data for porous PETN [21].

Table B3. Parameter input for DDT in PETN

NRHO	NTMP	ECON	PCON	RCON	A1S	A2S	A3S
56	12	4.184e-5	1.01325e-6	1.0	0.111	0.136	1.631
B0S	B1S	B2S	GAMMIN	CVS	IFCH	FB1M	FB2M
0.6	0.6	0.0	0.25	2.e-5	1.	0.2	0.8
ALPMX	FRQ	CQ	CL	QLIM	CQIN	CLIN	PCR
1.8	1.0	1.5	0.75	0.3	1.5e-4	0.06e-4	0.003
POWRC	T0	P0	POROS	RHO0	DIA	VELF0	POWF
3.0	300.	1.e-6	0.2126	1.778	0.018	0.01	0.66667
POWP	VALIG	IGVEL	NJIG	JIG1	…	JIG200	IDBG
1.0	195.	0.01	200	1	…	200	0
TDBUG	CC0	CC1	CC2	CC3	CC9	CC10	CC11
1.e6	4.e12	4.	8.e16	5.	1.0	3.e10	2.7
CC13	Bmax	Mmax	DFmax	IFWP	M2min		
0.0	0.	0.	0.	1.	0.		

Appendix C: History variable and concordance for HERMES versions 84a and higher

C.1 History variables available for plotting

Var#	Symbol	ALE3D name	Description
1	S/V	soverv	Specific surface area (surface to volume ratio)
2	Ignit	ignit	Ignition parameter
3	φ	porosity	Porosity
4	$\dot{\varepsilon}$	eps_dot_hermes	Local plastic strain rate
5	Ie2	int_eps_dot_2	Integral of the square of the plastic strain rate
6	$\langle\dot{\varepsilon}\rangle$	eps_dot_bar	Average plastic strain rate
7	μ	amu	Excess compression ρ/ρ_0 - 1

8	ifrac	ifrac	1 if element has fractured, 0 if not
9	minp	min_p_ever	Minimum pressure experienced by this element
10	workp	workpm	Plastic work per unit mass
11	λ	mass_frac_gas	Mass fraction burned
12	P	p_elem	Element pressure
13	P_g	p_gas	Gas pressure
14	P_s	p_sol	Solid pressure
15	P_{ads}	pad_sol	Pressure on solid principal adiabat
16	P_{mm}	p_mat	Macroscopic matrix pressure
17	P_{adm}	pad_mat	Pressure on matrix principal adiabat
18	e	em_elem	Element specific energy density (per unit mass)
19	e_g	em_gas	Gas specific energy
20	e_s	em_sol	Solid specific energy
21	e_{ads}	eadm_sol	Specific energy on solid adiabat
22	e_m	em_mat	Matrix specific energy
23	e_{adm}	eadm_mat	Specific energy on matrix principal adiabat
24	T_g	t_gas	Gas temperature (K)
25	T_s	t_sol	Solid temperature
26	T_m	t_mat	Matrix temperature
27	1/v	rho_elem	Element specific volume (per unit mass)
28	$1/v_g$	rho_gas	Gas specific volume
29	$1/v_s$	rho_sol	Solid specific volume
30	$1/v_m$	rho_mat	Matrix specific volume
31	wlim	wlim	Limiting value for recompression of expanded matrix
32	t_{ig}	tim_ig	Ignition time of an element
33	dt_{ig}	dtim_ig	Time for ignition to propagate through an element
34	qh	q_elem	Artificial viscosity for the element
35	Area		Element area (2D) or Volume (3D) LSDYNA only
36	Ncal		Number of ignition points used in ignition time calculation LSDYNA only
37	Porl	porl	Porosity under load (not unloaded to zero pressure)
38	Igsor	num_elem	1 for an element that has been an ignition source (LSDYNA) element number (ALE3D)
39	chi	s2_o_s1	Ratio of s_2/s_1, which is related to the Lode parameter
40	dvov	dvov_elem	logarithmic element volume strain
41	taum	tau_mat	Integral of Γ for matrix
42	zm	zm_mat	Entropy functional for matrix
43	alpha	alpha	Herrmann's alpha for matrix
44	alpha0	alpha0	"Starting" alpha for the matrix
45	taus	tau_sol	Integral of Γ for solid
46	zs	zm_sol	Entropy functional for solid
47	lambda1	lambda1	intermediate CREST model parameter

48	lambda2	lambda2	intermediate CREST model parameter
49	edot	edot_elem	total strain rate second invariant (for shear modulus calc)
50	cmedot	shmod	strain-rate dependent shear modulus
51	dworkp	dworkpm	increment of plastic work energy density
52	qintrin	qintrin	intrinsic artificial viscosity included in LS DYNA without user input. This is likely not to be needed for ALE 3D
53	Shearrho	shmod_rho	Shear modulus multiplied by current density for ALE 3D sound speed calculations
54	Bulkrho	blkmod_rho	Bulk modulus multiplied by current density
55	Rho	rho_elem1	density
56	Frdam	fr_dam	Damage from tensile fracture model of Ed Zywicz DYNA model #25
57	Frrvr	fr_vrel	Relative volume used in fracture model. This is defined as vm*rho0m/alpha, so that the fracture model only knows about volume relative to the initial porous condition
58	E	ale3d_ecc0	ALE3D energy per ref volume (read only)
59	V	ale3d_vrel	ALE3D relative volume (read only)
60	L	ale3d_el_elem	ALE3D distance across the element (for Q calculation, read only)
61	Vh-V	delta_vvo	Difference between post-advection relative volume from the HERMES history variable and ALE3D V
62	dvovg_1	dvovg1	dvov for the gas phase to achieve pressure equilibrium before burn changes λ
63	dvovg_2	dvovg2	dvov for the gas phase to achieve pressure equilibrium after burn changes λ
64	dvovg_r	dvovgr	dvov for the gas phase from post-advection fixup
65	Y	ystr_her	yield stress
66	M2	crest_m2	M2 parameter in CREST

C.2 Glossary for the input parameters (Table B2)

IF3D flag 0 for 2D (axisymmetric) 1 for 3D (not used in ALE 3D)

BULK bulk modulus. This is used to calculate the sound speed, so represents a safe value for compressed elements.

SHEAR shear modulus

EPS0 ε_0 used in specific surface area calculation

EPSPOW *pe* used in specific surface area calculation

EPSA *AA* used in specific surface area calculation

$$S/V = AA\left(\varepsilon - \varepsilon_0\right)^{pe}$$

SNORM σ_n, Normal stress used in ignition parameter

NORMP *pn*, power used in normal stress factor of ignition parameter

SHEARP *ps*, power used in shear factor of ignition parameter

$Ignit = \int\left(\frac{p - s_2/2}{\sigma_n}\right)^{pn}\left(2 - \frac{3|s_2|}{y}\right)^{ps} d\dot{\varepsilon}$, where *p* is pressure, s_2 is the intermediate principal stress deviator, and *y* is the yield stress.

TINIT Ambient temperature, used for shift in the strain-rate dependence

TSHIFT fraction of a decade shift per degree Kelvin different from ambient (293)

PHICR φ_c, used in the calculation of Ω

D *D* used in the calculation of Ω

CRES *Cr* slope of the residual strength curve

YC y_c, unconfined compressive strength parameter

S0 s_0 used in pressure-dependent strength calculation

M0 m_0 used in pressure-dependent strength calculation

N *n* used in pressure-dependent strength calculation

EPSH e_h used in strain-hardening term (δ)

EDOT0 $\dot{\varepsilon}_0$ used in strain-rate dependent term

EDPOW *p* used in strain-rate dependent term

C *C* used in strain dependent calculation

ARES *Ar*, the offset of the residual strength

Bten Ratio of the uniaxial tensile strength to the uniaxial compressive strength

A0 A_0 used in calculation of porosity increase with strain rate (bulking rate)

A1 A_1 used in calculation of porosity increase with strain rate

MINP Minimum pressure permitted before fracture (after fracture the value is zero).

The following may have been resolved, but should be checked:

Value has interactions with development of burn pressure. Calculations with a large tensile value of MINP do not burn the same as those with a smaller value. The pressurization of burn is delayed until the matrix tension exceeds MINP, then the pressure builds up. If burn-up is not required, then use a value of -0.0001 to 0.001 Mbar. This does a better job for the mechanical deformation. The fix for calculating burn-up will be delayed until after November. I will send it to John, who can advise on location of the executable.

MINY (NOT USED)

FAIL used to set failed element flag if element volume less than a minimum equal to λvgmin+(1-λ)vsmin. FAIL less than zero does not set the flag and stops the calculation. FAIL greater than or equal to one does set the flag and the calculation continues.

MAXIT maximum number of iterations permitted to solve for consistent plastic strain rate. If the criterion is exceeded, the calculation prints a message on *STDOUT* and stops.

TOL The criterion for a successful iteration for consistent plastic strain rate is that

$\left|3Gdt\dot{\varepsilon} + y(\dot{\varepsilon}, \varepsilon, p) - \tilde{\sigma}\right| < (TOL)y_c$, where $\tilde{\sigma}$ is the elastically incremented equivalent stress

TOLP The criterion for a successful iteration for pressure equilibrium

FMC Flag to calculate with the vonMises (0.) or Mohr-Coulomb (≥1) models

FIB Flag to calculate with isochoric burn (1, 2, 3, or 4) or incremental gas phase energy (0). Choices 2, 3, or 4 are required for the present implementation that requires CREST-lite to use the entropy parameter Z(S) calculated from the solid. Choice 4 is recommended strongly.

CMLOW rubbery modulus (shear modulus at low strain rate)

CMHIGH glassy modulus (shear modulus at high strain rate)

TAU time constant for calculating shear modulus

YSTRMX maximum yield stress permitted

IFA3D flag to decide on different code for ALE 3D (value 1) and LSDYNA (value 0).

FRSIGC Tensile fracture strength (maximum principal stress). If zero, fracture model is ignored. The value here is about 0.15 times the uniaxial compressive stress at a strain rate of 1 sec^{-1}

FRSCRIPG Fracture surface energy absorbed in creating new surface area. The value for CompB is taken from experiments by Ferranti (unpublished).

FRDXEL element size. Here is a chance to go wrong, especially in a mesh dependence study. The intent of the model is to foster mesh independence when the mesh size is smaller than a maximum determined by the other fracture parameters. Note that for fracture, the properties used are the quasi-static shear modulus, and (adiabatic) bulk modulus.

FRTOL The maximum damage permitted is 1-FRTOL. The stress is at least FRTOL*FRSIGC so never forced to zero. This is the δ in Zywicz's DYNA write-up.

FRSMLS This is nominally taken as 1/3, but can be otherwise specified. See Zywicz write-up.

C.3 Glossary for the parameter file (Table B3)

NRHO Number of density entries in the gas equation of state table

NTMP Number of isotherms in the gas equation of state table

ECON Conversion factor. Multiply cal/g to get desired energy density unit

PCON Conversion factor. Multiply atmospheres to get desired pressure unit

RCON Conversion factor. Multiply g/cm^3 to get desired density unit

A1S A1, linear parameter in the polynomial form solid principal adiabat of the reactant

A2S A2, quadratic parameter of the solid.

A3S A3, cubic parameter of the solid

B0S B0, parameter in Grüneisen term

B1S B1, parameter in the JWL form for the solid

B2S B2, quadratic parameter in the Grüneisen

$$P_S = A_1\mu + A_2\mu^2 + A_3\mu^3$$

$$\frac{\Gamma}{v} = \rho_0(B_0 + B_1\mu + B_2\mu^2)$$

$$P = P_s + \Gamma(e - e_s)/v$$

GAMMIN Minimum value of Γ

CVS c_v, Specific heat of the solid per unit reference volume

IFCH 1 uses the Carroll-Holt modification of the P-α model, 0 does not.

FB1M, FB2M parameters to reduce the stiffness of the unload-reload curve

$$f_b = f_{b1} + f_{b2}(\alpha_x - \alpha)/(\alpha_x - 1)$$

where α_x is ALPMX

ALPMX maximum value of Herrmann's that permits matrix strength. Setting this parameter much larger than the initial value consistent with the initial porosity results in a large, reversible pressure change before irreversible crushing occurs. This would be appropriate for pressed formulations, but not for cast formulations or poured powder.

FRACQ fraction of the artificial viscosity allotted to the matrix. The value 1 is strongly recommended.

CQ C_q, coefficient for the quadratic artificial viscosity

CL C_l, coefficient for the linear artificial viscosity

$$qh = 0, \quad \frac{\dot{v}}{v} \geq 0$$

$$qh = C_q^2 l^2 / v \left(\frac{\dot{v}}{v} \right)^2 - C_l a l / v \frac{\dot{v}}{v}, \quad \frac{\dot{v}}{v} < 0$$

$$l = \sqrt{Area}, \quad 2D$$

$$l = \sqrt[3]{Volume}, \quad 3D$$

where v is the specific volume and a is $\sqrt{P/\rho}$.

In ALE 3D the parameter l is passed to HERMES in history variable 34.

QLIM Maximum value of viscosity permitted

CQIN the intrinsic quadratic coefficient of the artificial viscosity (used by LS DYNA and set with the *CONTROL_BULK_VISCOSITY parameter cq)

CLIN the intrinsic linear coefficient of artificial viscosity (used by LS DYNA and set with the *CONTROL_BULK_VISCOSITY parameter cl)

PCR P_c, the crush pressure of the matrix at which all porosity is gone.

POWRC pc, power for the crush curve

$$P_{crush} = P_c \left[1 - \left(\frac{\alpha - 1}{\alpha_0 - 1} \right) \right]^{1/pc}$$

T0 Initial temperature. For consistency, set this no lower than the first temperature entry in the EOS table for the gas products.

P0 Initial pressure

POROS φ, initial porosity (gas-filled volume/total volume) Use 0.001 for the solid. When used in *ALE3D*, the initial density may be specified as a function of position in the *REGION* block. The porosity and other associated variables will be set properly, but in this case the POROS parameter must take the value of the smallest porosity in the region. In the remap step, that value is enforced as the floor value for porosity.

RHO0 ρ_0, reference density of the solid

DIA d, equivalent sphere diameter for the desired surface to volume ratio

$\frac{S}{V} = \frac{6}{d}$ at time zero. If using S/V calculation to calculate DIA, set to 0, unless the material is initially granular. For that case the specific surface area used in calculating the mass burn rate is the larger of 6/*d* and the *S*/*V* damage calculation.

VELF0 v_0, laminar flame speed for unit pressure

POWF pf, power for mass fraction dependence of laminar flame speed, v_l

POWP pp, power for pressure dependence of laminar flame speed

$$v_l = v_0 (1-\lambda)^{pf}\, p^{pp}$$

IGVAL Value of the ignition parameter (Ignit) to initiate burn . This value is is mesh dependent and dependent on the friction coefficient. With a radial mesh size 0.033 cm and axial mesh size 0.06 cm, the value 195 gives ignition at the correct velocity for LLNL and UK Steven tests. When geometrically similar meshes are used, the ignition parameter is 340exp(-Δr/0.062 cm) for a friction coefficient of 0.4, based on calculations of the UK test geometry with radial meshes of 0.01 to 0.066 cm. Use a large number, say 700, to suppress ignition. In ALE-3D this value is ignored. Instead, the value is input in the CHEMISTRY block.

VELIG Velocity of flame propagation through the porous solid. This should be (considerably) less than the sound speed of the hot gas, which is about 0.1 cm/μs. The velocity should depend on the porosity, the specific surface area, and the gas pressure gradient, but is a constant in the present version. In ALE-3D this value is ignored. Instead, the value is entered in the CHEMISTRY block.

NJIG number of elements (LS-DYNA) assumed to be ignited at time zero (no more than about 1500, because the current dimension of the eosp array is set to 1600) Ignored in ALE-3D, which initializes this in the REGION block and uses level-set to propagate burn.)

JIG1 element number of the first ignited element

JIGN element number of the NJIGth ignited element

IDBUG external element number desired for debug print statements that include each iteration in the approach to pressure equilibrium each cycle, and each iteration for strength calculation. Needless to say, this can be an overwhelming amount of output. To suppress for both LS DYNA and ALE 3D use -1

TDBUG time at which to begin debug prints. To suppress, use a time larger than the problem end time, for example 1 second.

CC0, CC1, CC2, CC3, CC9, CC10, CC11, CC13 Input parameters for CREST Lite model. Setting CC13 to a large positive value suppresses detonation.

$$Z_s = \max(0, Z - c_{13})$$

$$b_1 = c_0 Z_s^{c1}$$

$$b_2 = c_2 Z_s^{c3}$$

$$m_2 = c_{10} Z_s^{c11} (1-\lambda) b_2^{-0.5}$$

$$\dot{\lambda}_1 = (1-\lambda_1)\sqrt{-2 b_1 \ln(1-\lambda_1)}$$

$$\dot{\lambda}_2 = \lambda_1 (1-\lambda_2)\sqrt{2 b_2 [\lambda_1 b_2 / b_1 - \ln(1-\lambda_2)]}$$

$$\dot{\lambda}_c = m_2 \dot{\lambda}_2$$

In the implementation the total rate of change of λ is the sum of the CREST $\dot{\lambda}_c$ and that

from HERMES burning. The parameters b_1 and b_2 have dimensions the square of reciprocal time. The parameter m_2 has dimension reciprocal time.

Bmax maximum value of the b1, b2 parameters permitted. Note this is imposed after the m2 parameter is calculated but before the λ1, λ2 parameters are calculated, in accord with the PERUSE implementation. Input the value of zero to have no limits on b1, b2.

Mmax maximum value of m2. Input the value zero to have no limit on m2.

DFmax maximum increment of the burn fraction λc. Input zero to have no limit on λc.

IFWP 0 – include plastic work in Z calculation; 1 – do not include plastic work

M2min Minimum value of the CREST m2 parameter permitted